Journal of Alloys and Compounds 934 (2023) 167887

Contents lists available at ScienceDirect

Journal of Alloys and Compounds

journal homepage: www.elsevier.com/locate/jalcom

Research Article

Achieving high energy storage density simultaneously with large efficiency and excellent thermal stability by defect dipole, and microstructural engineering in modified-$BaTiO_3$ ceramics

Mahmoud.S. Alkathy [a,b,*], Attaur Rahaman [a], Valmor R. Mastelaro [c], Fabio.L. Zabotto [a], Flavio Paulo Milton [a,d], J.A. Eiras [a,**]

[a] Physics Department, Federal University of São Carlos, São Carlos, SP 13565-905, Brazil
[b] Department of Physics, Faculty of Education & Science, Al-Baydha University, Baydha, Yemen
[c] Institute of Physics University of São Paulo, São Carlos, CEP 13566-590 São Carlos, SP, Brazil
[d] Federal University of Grande Dourados Faculty of Exact Sciences and Technology, FACET Applied Optics Group (GOA) Dourados, MS 79825-070, Brazil

ARTICLE INFO

Article history:
Received 22 July 2022
Received in revised form 26 October 2022
Accepted 2 November 2022
Available online 3 November 2022

Keywords:
Co-doping
Grain size
Defect dipoles
Relaxor ferroelectric
Energy storage
Energy efficiency

ABSTRACT

The electric energy produced from renewable sources can assist in shifting to clean energy. An efficient energy storage system is needed to use this energy for an appropriate time. High breakdown strength (E_b) and a significant difference between (P_{max}) and (P_r) are required to achieve this goal. Here double-hysteresis-loop ceramics with different polarization are achieved by B-site co-doping engineering to control the defect structure. According to the structural analysis, the (Ni^{2+}, Cu^{2+}), (Mg^{2+}, Cu^{2+}), and (Mg^{2+}, Ni^{2+}) co-dopant ions were successfully incorporated into the BTO unit cell. Results show that the sample co-doped with Mg^{2+} and Ni^{2+} exhibits the apparent characteristics of a double hysteresis loop, higher polarization, and more considerable breakdown strength (E_b). This behavior was explained based on the defective dipoles' formation. Low valence (Ni^{2+}, Cu^{2+}), (Mg^{2+}, Cu^{2+}), and (Mg^{2+}, Ni^{2+}) ions co-substitute Ti^{4+} ions to form $(M_{Ti}'' - V_O^{\bullet\bullet})^{\times}$; [M= Mg^{2+}, Cu^{2+}, Ni^{2+}] defect dipoles with neighbouring oxygen vacancies. The domain wall was pinned by the defect dipoles and prevented from moving by the oxygen vacancies, resulting in a pinched hysteresis loop that resembles the double hysteresis loop found in antiferroelectric materials. A high energy storage density and efficiency are thereby produced. At an electric field of 159 kV/cm, the BMNT sample displayed an energy storage density (W_{rec}) of 1.585 J/cm^3, which was around 6 times more than that of the pure sample, and an efficiency (η) of about 94%. The BMNT sample is also exceptionally stable over a range of temperatures and frequencies, making them a good candidate for applications in the field of energy storage in the future.

1. Introduction

Electroceramics materials are considered as one of the promising materials for fabricating energy storage devices that can be used in various applications such as pulsed power systems [1–3]. Non-functionally, the energy storage performance of dielectric capacitors made of ceramic materials is much less than the needs of energy storage systems, especially the low efficiency of their operation in the high-temperature range [2,4]. The researchers working in the field of energy storage developments are looking for dielectric materials that show high energy storage density (W_{rec}), high energy storage efficiency (η), and good thermal stability to meet the requirement of energy storage applications [4–6]. At the same time, the high value of W_{rec} can be exploited in the weight reduction and integration of ceramic dielectric capacitors [4,5]. Additionally, the high-efficiency value can be used to reduce the thermal production of dielectric capacitors during the charging and discharging process and thus enhance the reliability of the energy storage systems. Furthermore, concerning thermal stability, its benefit lies in its ability to give the capacitors a distinctive operational ability even at high temperatures without the need to use any cooling systems to cool them. Multiple studies have been carried out to explore unique energy storage materials based on dielectric ceramics with large energy storage density (W_{rec}), high efficiency (η), and good thermal

* Corresponding author at: Physics Department, Federal University of São Carlos, São Carlos, SP 13565-905, Brazil.
** Corresponding author.
E-mail addresses: alkathy@df.ufscar.br (M.S. Alkathy), eiras@df.ufscar.br (J.A. Eiras).

https://doi.org/10.1016/j.jallcom.2022.167887
0925-8388/

stability simultaneously. Despite all these attempts, significant progress in this field to obtain those materials that have the properties mentioned above is still in progress. Therefore, it has become necessary to work continuously on the examination and exploration of new ceramic materials that have good storage properties and a large energy storage density (W_{rec}). In terms of fundamental physics, the energy storage density (W), recoverable energy (W_{rec}), and energy storage efficiency (η) can be represented by the following formulas [4–7].

$$W = \int_0^{P_{max}} PdE \tag{1}$$

$$W_{rec} = \int_{P_r}^{P_{max}} PdE \tag{2}$$

$$\eta = \frac{\int_{P_r}^{P_{max}} PdE}{\int_0^{P_{max}} PdE} \tag{3}$$

The P_r in these formulas is defined as the remnant polarization, P_{max} is the maximum polarization, and E is the applied electric field. According to the above formulas, the most desired materials for high energy storage density have a large breakdown strength (E_b), high P_{max}, and low P_r. In terms of energy storage development, several types of bulk ceramics, such as linear dielectrics, ferroelectrics, relaxor ferroelectrics, and antiferroelectric, can be utilized [4,5,8–11]. The main goal of obtaining high energy storage properties is to create defect dipoles in the lattice or improve polarization performance by developing relaxed dielectrics (RFEs) from nonlinear dielectrics. Although lead-based ceramics have excellent energy storage properties, for example $(Pb_{0.98}La_{0.08})(Zr_{0.91}Sn_{0.09})O_3$ with an energy storage density of 3.04 J/cm^3 and an efficiency of 92% at 170 kV/cm, but unfortunately, the toxicity of lead causes environmental and health concerns that limit its use in practical applications [12]. Hence, exploring the green virtues of energy storage ceramics is necessary. The $BaTiO_3$ (BTO) ferroelectrics have become a target and attractive material in the fields of energy storage due to their BDS moderation and their properties of polar domains and large energy barriers in the switching field [13–15]. By single and/or co-doping the host lattice of BTO, the long-range ordered micrometer size is converted into short-range–ordered nanodomains with increasing local inhomogeneity in RFEs [16–19]. The shrinkage of the domain size and the weakening of the domain intercoupling reduce the field-switching energy barriers, resulting in a pinched hysteresis loop and improving the energy storage properties in relaxor ferroelectrics RFEs [20]. Many relaxor ferroelectrics based on environment-friendly bulk ceramics of $BaTiO_3$ are extensively studied regarding energy storage developments [21–25]. Illustrative examples, Dong, Xi et al. et al. [21] obtained a recoverable energy storage density in 0.93BT− 0.07YNb ceramics of 0.614 J/cm^3 and efficiency of 87% at 173 kV/cm. Liu, G et al. found [25] a recoverable energy storage density in MgO-doped $BaTiO_3$ ceramics of 0.90 J/cm^3 and an efficiency of 73% at 130 kV/cm. The better energy storage density of 2.41 J/cm^3 at 230 kV/cm coupled with a high energy efficiency of 91.6% has been reported by M. Zhou et al. [26] in $0.85BaTiO_3$-$0.15Bi(Zn_{0.5}Sn_{0.5})O_3$ ceramics, while the discharge energy density was 0.47 J/cm^3 at 110 kV/cm. Dan Meng et al. [27] achieved a high energy density of 3.27 J/cm^3 with excellent thermal stability in the $0.92BaTiO_3$-$0.08La(Zn_{0.5}Hf_{0.5})O_3$ ceramics at 480 kV/cm, while the W_{rec} was close to 1 J/cm^3 at 150 kV/cm.

The doping of the A-site and B-site of $BaTiO_3$ host lattice with foreign ions having different valences and radii resulted in breaking the long-range ferroelectric order and forming polar nano-regions (PNRs). Permittivity-temperature curving may massively broaden and flatten as a result of this phenomenon. Also, most previous reports on energy storage properties investigated only the energy properties at room temperature. Only a few studies examine the energy storage performance over a broad scope of temperatures. The energy storage features as a function of temperature can be considered an essential task needed to operate ceramic capacitors within a wide range of temperatures without affecting their efficiency. Thus, the objective of extending the temperature stability for energy storage applications remains a significant challenge. The relaxor ferroelectric is a valuable material for developing the thermal stability of energy storage properties.

From the point of view of our knowledge, most of the previous studies focused on the enhancement of the breakdown strength (E_b) to enhance the energy storage density. Few researchers paid attention to increasing the difference between P_{max} and P_r values [28–32]. It is known that the defect dipoles significantly impact the development of the energy storage performance of relaxor ferroelectric [28–36]. The defect dipoles can create a defect dipoles moment (P_d), acting as an internal field to switch the new domain back to its original state when the electric field is removed. The defect dipoles created by B-site acceptor doping are thought to have the ability to improve the energy storage performance of the BTO ceramic.

In this work, the (Ni^{2+}, Cu^{2+}), (Mg^{2+}, Cu^{2+}), and (Mg^{2+}, Ni^{2+}) ions have been selected to co-doped $BaTiO_3$ ceramics aiming to enhance the energy storage performance. The co-doping samples exhibit a pinching hysteresis loop resulting in a lower remanent and a higher maximum polarization. Moreover, the breakdown strength and energy storage density have been improved. The reasons for pinching in electric hysteresis loops need further study and deep understanding. The novelty of this work lies in accelerating the exploration of higher-performance lead-free dielectric materials and providing a deeper understanding of the relationship between defects dipoles, physical properties, and energy storage performance. Herein, a high energy storage density (1.585 J/cm^3) accompanied by an ultrahigh-energy storage efficiency (94%) was observed in the (Mg^{2+}, Ni^{2+}) co-doped $BaTiO_3$ [BMNT] ceramic. In addition, the [BMNT] ceramic shows excellent temperature stability of its energy storage properties in the temperature range of (25–120 °C) due to the relaxor-like behavior. The obtained results not only indicate the superior potential of environment-friendly $BaTiO_3$-based relaxor-like ferroelectric ceramics for the design of ceramic capacitors capable of high energy storage but also promising for improving the thermal stability of energy storage properties.

2. Experimental

In this work, we synthesized $Ba[Mg_{0.50}Cu_{0.50}]_{0.10}Ti_{0.90}O_3$, $Ba[Ni_{0.50}Cu_{0.50}]_{0.10}Ti_{0.90}O_3$, and $Ba[Mg_{0.50}Ni_{0.50}]_{0.10}Ti_{0.90}O_3$ abbreviated as [BMCT], [BNCT] and [BMNT] ceramics using conventional solid-state reaction method. The starting powders $BaCO_3$, MgO, CuO (Sigma-Aldrich, 99.99% purity), NiO (Sigma-Aldrich, 98.99% purity), and TiO_2 (Sigma-Aldrich, 99.8% Purity) were weighed, and ball milled for 24 h and subsequently calcined at 1100ºC, using a conventional furnace with heating/cooling rates of 5 °C/min and dwell time of 8 h. Once again, the calcined powders were ball milled for 24 h and sieved to homogenize the particle size. After that, green pellets of 10 mm diameter and 1 mm thickness were made with a few drops of binder Polyvinyl Alcohol (PVA). To get rid of the binders in the samples under study, the green pellets slowly heated at a rate of 2 °C/min, until reaching 500 °C, and kept at this temperature for an hour. Consequently, the green ceramic of pure sample was heat treated at 1450 °C and the co-doped samples at 1300 °C for 4 h in the air with a heating and cooling rate of 5 °C/min. XRD (Bruker D8 system), Raman spectroscopy (Raman T64000 Jobin-Yvon Spectrophotometer with excitation source of (Ar-laser) 488 nm wavelength and spectra collection through CCD camera, and SEM were carried out to analyze the structural properties of the sintered samples. X-ray Photoelectron Spectroscopy (XPS) for the BMNT sample was carried out using the Scienta Omicron

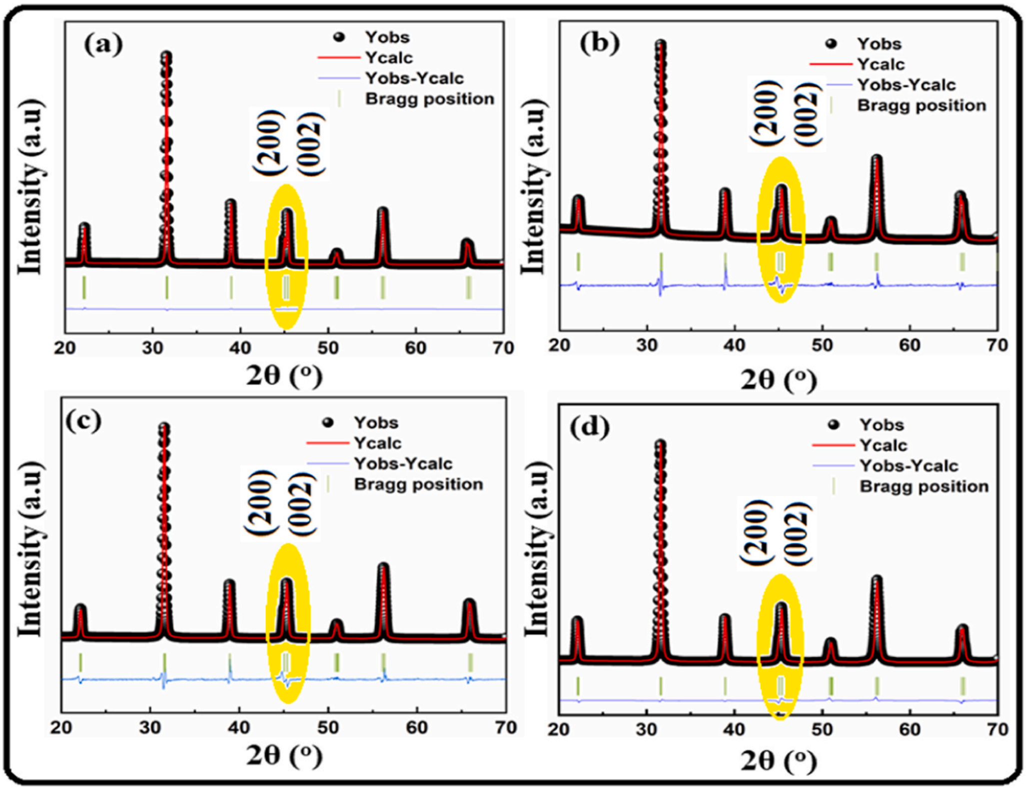

Fig. 1. : Structural refinement of the (a) BTO, (b) BNCT, (c) BMCT, and (d) BMNT ceramics achieved using Fullprof refinement.

ESCA+ spectrometer with monochromatic X-ray source Al-Kα (1486.7 eV, with a power of 280 W and a constant pass energy mode of 50 eV). At room temperature, the ferroelectric tests were carried out with a homemade apparatus based on a sawyer-tower circuit.

3. Result and discussion

The XRD analysis of BTO, BNCT, BMCT, and BMNT ceramics are achieved using Fullprof refinement, as shown in Fig. 1(a)-(d), respectively. The obtained lattice parameters are recorded in Table 1. All investigated samples exhibit a typical perovskite structure well-matched with the tetragonal phase of standard $BaTiO_3$ (JCPDS file no: 01–079–2265) [37]. No secondary phase is detected in all investigated samples, indicating that (Ni^{2+}, Cu^{2+}), (Mg^{2+}, Cu^{2+}), and (Mg^{2+}, Ni^{2+}) ions have successfully incorporated into the BTO lattice, and form BNCT, BMCT, BMNT compounds. From Fig. 1, it is clear that the splitting of 200 peaks at (2θ) 44–46° turn to a single merged peak in the case of (c) BMCT and (d) BMNT. The (200) peak's merger suggests the tetragonality decreases appreciably, and the phase begins to shift from a tetragonal phase to a pseudo-cubic phase. The merging of separated peaks leads to the broadening of the diffraction peaks, demonstrating a decrease in crystallite size. The merging of diffraction peaks indicates distortion in the structure, which may be attributed to the difference in ionic radii of (Mg^{2+}[0.72 Å], Ni^{2+}[0.690 Å]), and (Ti^{4+}[0.605 Å, 6 CN]. Moreover, the merger of the (002) (200) peaks proves that the crystal lattices' tetragonal phase has a relaxation behavior. This relaxation correlated with the shrinkage of the *P-E* hysteresis loops and significantly improved energy storage performance due to a substantial difference between (P_{max}) and (P_r), as seen in the energy storage discussion. As shown in Fig. 1(b), the lattice distortion brought on by the incorporation of (Mg^{2+}, Cu^{2+}), and (Mg^{2+}, Ni^{2+}) is thought to be the cause of the merging of the (200) and (002) peaks. It is well knowledge that elements with comparable ionic radii can quickly replace one another [38]. Since the (Mg^{2+} [0.72 Å], Cu^{2+} [0.73 Å]), (Ni^{2+} [0.690 Å], Cu^{2+} [0.73 Å]), (Mg^{2+} [0.72 Å], Ni^{2+} [0.690 Å]) having ionic radius greater than (Ti^{4+} [0.605 Å, 6 CN], and lower than Ba^{2+} [1.61 Å, 12 CN) [39]. From the peak shifting shown in Fig. 2(b), it might prove that the co-dopant ions partially occupy the Ba^{2+} site and Ti^{4+} site in the $BaTiO_3$ host lattice. The fluctuation of the lattice constants [Ref Fig. 2(c)] of the co-doped samples also may be due to the fact that some of the co-dopant ions may be replaced at the Ba^{2+} site, which has large ionic radii. Fig. 2(a) illustrates the oxygen vacancy induced due to the valence mismatch between (Mg, Ni) ions and Ti. From Fig. 2(d), the tetragonality (c/a) is increased for the (Mg^{2+}, Cu^{2+}) co-doping and consequently decreased for the (Ni^{2+}, Cu^{2+}) and (Mg^{2+}, Ni^{2+}) co-doping samples which could be confirmed by weakening the (200) and (002) peak splitting. The split in the XRD peaks is more pronounced for pure BTO and BNCT ceramics with larger grain sizes. The coherently diffracting domain size is assumed to be the

Table 1
Estimated parameters from Rietveld refinement for pure and co-doped ceramics.

Sample	BTO	BNCT	BMCT	BMNT
Crystal System	Tetragonal	Tetragonal	Tetragonal	Tetragonal
a=b (Å)	3.9979	3.9974	3.9980	3.9968
c (Å)	4.0292	4.0259	4.0258	4.0242
c/a	1.007829	1.00713	1.006953	1.006855
V (Å)^3	64.3990	64.3309	64.3484	64.2847
Space group	P4mm	P4mm	P4mm	P4mm
SG No.	99	99	99	99
Theoretical density g/cm^3 obtained from XRD	6.107	6.183	6.195	6.0188
Measured Density g/cm^3	5.563	5.874	5.824	5.718
Relative density (%)	94.37	96.56	95.55	95.00
D_p (nm)	76.22	81.31	57.14	53.18
R_p (%)	2.27	3.19	7.64	3.83
R_{wp} (%)	3.39	3.65	3.97	4.93
R_{ex} (%)	2.48	2.96	2.57	3.49
χ2	1.868	1.519	2.386	1.995

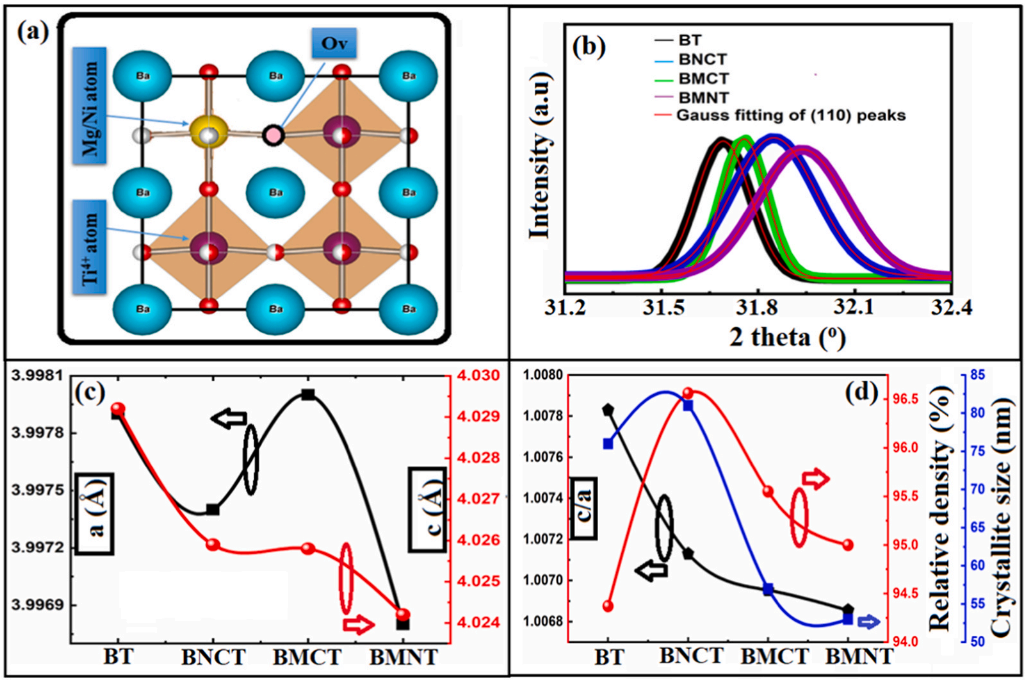

Fig. 2. (a) represents a schematic diagram of the crystal structure of the BMNT sample, (b) an enlarged view of (110) peak along with Gaussian fitting for all investigated samples, (c) Representation of unit cell parameters (a, c) of different compositions, and (d) represent the tetragonality (c/a), relative density, and crystallite size of different compositions.

crystallite size (D_p), which is not necessarily the same as the particle size. We estimate the average crystallite size (D_p) of the samples by substituting the values of the full width at half maximum (*FWHM=β*), and Bragg diffraction angle (θ) induced from the gaussian fitting of the (110) peaks [as Referring in Fig. 2(b)] on the Debye-Scherrer equation [40,41]:

$$D_p = \frac{K\lambda}{\beta cos\theta} \quad (4)$$

where K is Scherrer's constant (0.89), and λ is the wavelength of the X-ray radiation (1.5406). The obtained average crystallite size is recorded in the Table 1, and it is found to increase from 76.22 nm to 81.31 nm for BNCT sample and then decrease to 57.14 nm and 53.18 nm for BMCT and BMNT respectively as depicted in Fig. 2(d). From Fig. 2(d), the relative density decreases in the samples BMCT and BMNT. This implies that the oxygen vacancy increases in these two samples resulting in generated pores in these specimens, as we can see in the SEM images.

Raman spectroscopy was used to supplement X-ray diffraction data by revealing molecular and crystal structures, local distortions brought on by changes in ionic radius between the host material and the dopants, and potential low-concentration contaminants missed by the latter [42]. Fig. 3(A)(a)-(d) shows the Raman spectra of the pure and co-doped $BaTiO_3$ ceramics with (Ni^{2+}, Cu^{2+}), (Mg^{2+}, Cu^{2+}), and (Mg^{2+}, Ni^{2+}), along with their spectral deconvolution into Lorentzian-shaped peaks studied at room temperature. According to group theory, the tetragonal phase of barium titanate consists of four fundamental modes designated as $A_1(TO_2)$ mode, sharp peak $E(TO_3)$ mode, $A_1(TO_3)$ mode, and $A_1(LO)$ mode at various locations between 270 cm^{-1} and 720 cm^{-1} [43]. The BNCT, BMCT, and BMNT ceramics display modes are comparable to BTO Raman spectra. The presented modes in pure and co-doped samples can be summed up as $E(TO_2)$ mode at the wavenumber range of 180–200 cm^{-1}, which is connected to the displacement of the Ba-O vibration modes, modes $A_1(TO_2)$, $E(TO_3)$, and $E(LO_3)$] observed at the wavenumber range of 270–340 cm^{-1}, linked to the displacement of the (Ti/M)-O; M= (Ni^{2+}, Cu^{2+}), (Mg^{2+}, Cu^{2+}), and (Mg^{2+}, Ni^{2+}) vibrations modes, The $A_1(LO_3)$ mode, visible at about 720 cm^{-1} is then attributed to octahedral distortion in ferroelectric phase, followed by the $A_1(TO_3)$ mode [44–46]. Fig. 3(a) makes it obvious that the sharp peak $E(TO_3)$ at 310 cm^{-1} intensities decreases after simultaneously denoting the tetragonality, which is consistent with the XRD data. The broad bands in the samples under investigation Fig. 3(a-d) result from various modes merging with others. It is interesting to see in Fig. 3 how the introduction of (Ni^{2+}, Cu^{2+}), (Mg^{2+}, Cu^{2+}), and (Mg^{2+}, Ni^{2+}) ions into the Ti^{4+} site caused the shifting of the Raman modes, as shown in Table 2, which could be attributed to an octahedral distortion or Ti cation displacement [47–50]. When an ion with a smaller/bigger ionic radius, such as (Mg^{2+} [0.57 Å], Cu^{2+} [0.73 Å], (Ni^{2+} [0.690 Å], Cu^{2+} [0.73 Å], or (Mg^{2+} [0.57 Å], Ni^{2+} [0.690 Å] co-doped (Ti^{4+} [0.605 Å] [39], the Raman modes shifting can be expected.

Additionally, the $A_1(LO_3)$ mode appears to be decreasing, which might have resulted from a considerable distortion and cationic disorder induced by co-doping [51]. This leads to the conclusion that octahedral distortions and cationic disorder are caused by B-site ions dispersed randomly within the octahedron. The supercells of pure BTO and BMNT samples were designed using VESTA software in order to further evaluate the detailed effects of B-site co-doping on the crystal structure, as shown in Fig. 3(C). After Mg^{2+} and Ni^{2+} co-doping, the tetragonality value of the BMNT super cells (1.00686) is lower than that of pure BTO super cells (1.00783), supporting the Raman spectra results in Fig. 3(A) and (B).

Fig. 4, shows the SEM images of the pure and (Ni^{2+}, Cu^{2+}), (Mg^{2+}, Cu^{2+}), and (Mg^{2+}, Ni^{2+}) co-doped $BaTiO_3$ samples. Clearly, the pure BTO sample shows a highly dense microstructure with large grains. There is no difference in the morphological structure between the pure BTO sample and the BNCT sample, confirming the phase

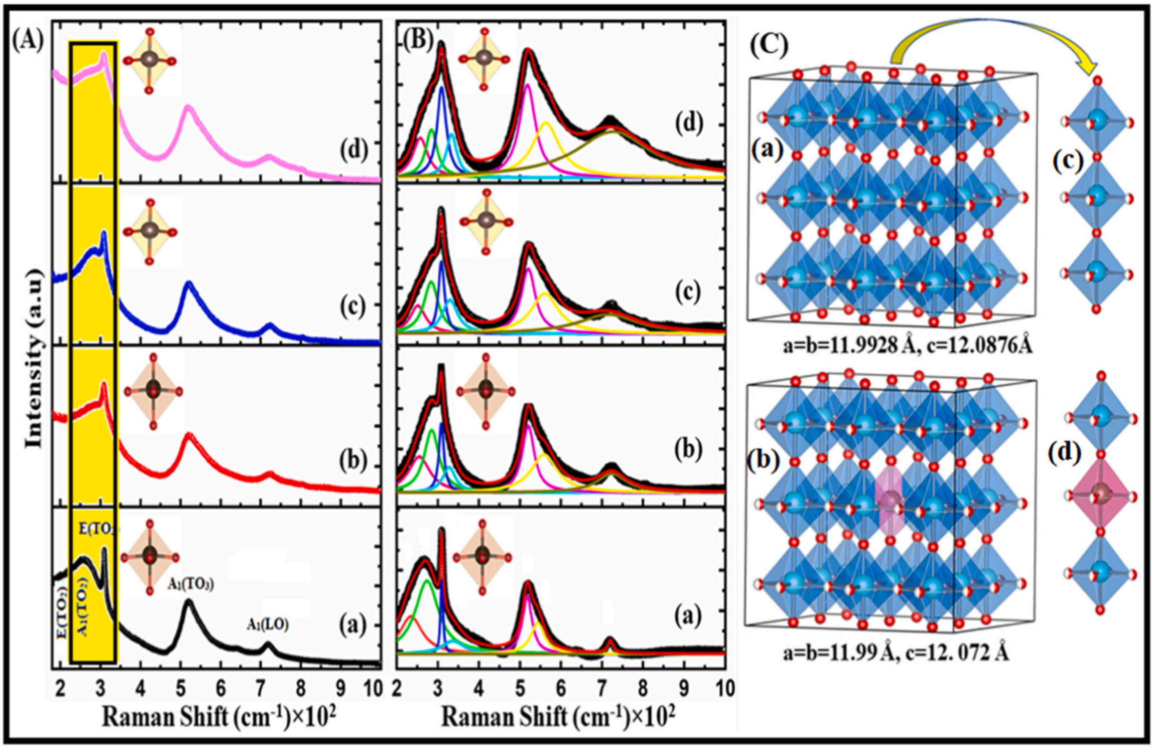

Fig. 3. : (A) Room temperature Raman spectrum of (a) BaTiO3, (b) BNCT, (c) BMCT, and (d) BMNT sintered samples along with (B) unconvoluted each broad mode into their components after baseline correction, and (C) Superlattice structure of (a) pure BTO, (b) BMNT. The right graph in (C) represented the [001] direction of (c) pure BTO and (d BMNT ceramics.

Table 2
Fundamental frequencies (cm^{-1}) with their symmetry modes, and full width half maximum obtained from Raman modes fitting for pure and co-doped materials.

Sample	BTO	BNCT	BMCT	BMNT
Wavenumber of $E(TO_3)$ mode (cm^{-1})	310.02	309.02	309.06	309.60
Wavenumber of $A_1(TO_3)$ mode(cm^{-1})	517.47	520.01	520.09	518.09
Wavenumber of $A_1(LO)$ mode (cm^{-1})	720.37	723.62	715.11	726.79
FWHM of $E(TO_3)$ mode (cm^{-1})	7.43	15.23	18.26	27.29
FWHM of $A_1(TO_3)$ mode (cm^{-1})	28.48	36.27	42.13	47.33
FWHM of $A_1(LO)$ mode (cm^{-1})	16.11	87.30	177.52	221.18

structure is not affected after co-doping. Comparing Fig. 4(c) and (d) with (a) and (b), we can see that the number of small grains increases, whereas the number of big grains decreases with (Mg^{2+}, Cu^{2+}), and (Mg^{2+}, Ni^{2+}) co-doping. In addition, porous microstructures occur for the sample with (Mg^{2+}, Cu^{2+}), and (Mg^{2+}, Ni^{2+}) co-doping. The average grain size was measured using the ImageJ software. The average grain size of the pure and co-doped samples in Fig. 4(a)-(d) were 6.524 µm, 6.451 µm, 4.570 µm, and 1.605 µm, respectively. That is to say, the grain sizes of $BaTiO_3$ ceramics decreased with co-doping. When Ni^{2+} and Mg^{2+} ions are co-doped in the BTO host lattice, there is a noticeable reduction in grain size. This finding indicates that (Mg^{2+}, Ni^{2+}) co-doping, which may be used as a grain growth inhibitor, suppresses the grain growth of BTO ceramics. This is because the incorporation of Ni^{2+} and Mg^{2+} ions resulted in the creation of oxygen vacancies. At the same time, the formed oxygen vacancies introduce movement into the crystal lattices, which may consume some energy.

Nonetheless, energy consumption helps the separation of solutes at the grain boundaries. Ni^{2+} and Mg^{2+} ions counteract boundary movement, positioning themselves at the grain boundaries and inhibiting grain growth. The smallest grain size in BMNT results in a diffused phase transition, high energy storage density, and high energy storage efficiency. Also, the small grain size and high relative density achieved under co-doping significantly enhance the breakdown strength, as we can see in the next section's discussion.

The XPS technique can determine the various oxidation states of the constituent parts of a chemical. The XPS Study was carried out for the optimum BMNT sample. Fig. 5(a), (b), (c), (d), and (e), respectively, show high-resolution XPS spectra of the Ba 3d state, Ti 2p state, O1s state, Ni 2p state, and Mg 2p state of the BMNT sample. The binding energies of Ba $3d_{5/2}$ and Ba $3d_{3/2}$ are 778.14 and 793.42 eV, respectively, which agrees with other reports [52]. In Fig. 5(b), you can see the XPS spectrum of Ti 2p. Peak spectra of Ti^{4+} $2p_{3/2}$ and Ti^{4+} $2p_{1/2}$ indicate that binding energies are found at 456.11 and 461,95 eV, respectively, which is consistent with the binding energies reported for TiO_2. Further confirmation of the oxidation state of Ti^{4+} comes from the spin-orbital splitting energies between the Ti^{4+} $2p_{3/2}$ and Ti^{4+} $2p_{1/2}$ peaks, being 5.84 eV. Two other signals were observed at binding energies of 455.33 and 460.11 eV, referred to as Ti^{3+} $2p_{3/2}$ and Ti^{3+} $2p_{1/2}$, respectively [53] Ti^{3+} concentration was estimated using the formula reported in reference [54,55] and was found to be 0.38. As a result, it can be concluded that a significant amount of Ti^{3+} is present in Mg^{2+} and Ni^{2+} co-doped $BaTiO_3$ ceramics. In addition, this illustrates the impact of oxygen vacancies and Ti^{3+} defects on the ferroelectric properties of BMNT ceramics. This leads to defects dipoles [56], which pin domain walls and cause the hysteresis loop pinching, which leads to an improved energy storage efficiency, as we will see in the next section. Fig. 5(c) shows that the O 1 s peaks (Ref. 4b) contain two prominent peaks at around 529.23 eV, corresponding to oxygen in

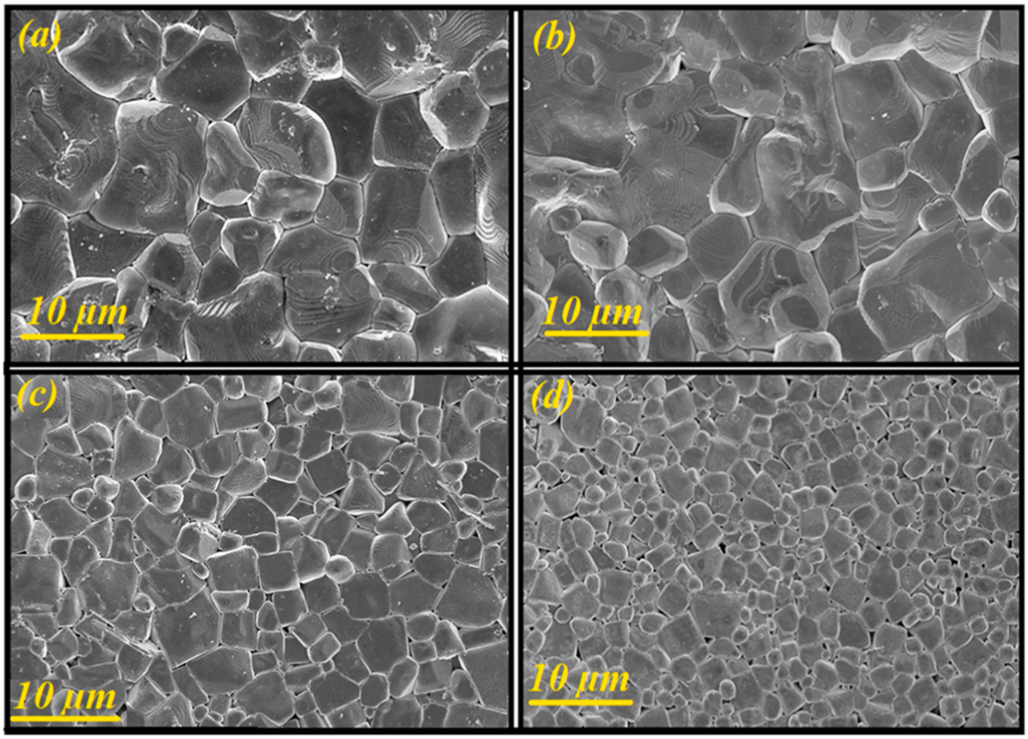

Fig. 4. : SEM images of the microstructure of (a) $BaTiO_3$, (b) BNCT, (c) BMCT, and (d) BMNT sintered samples.

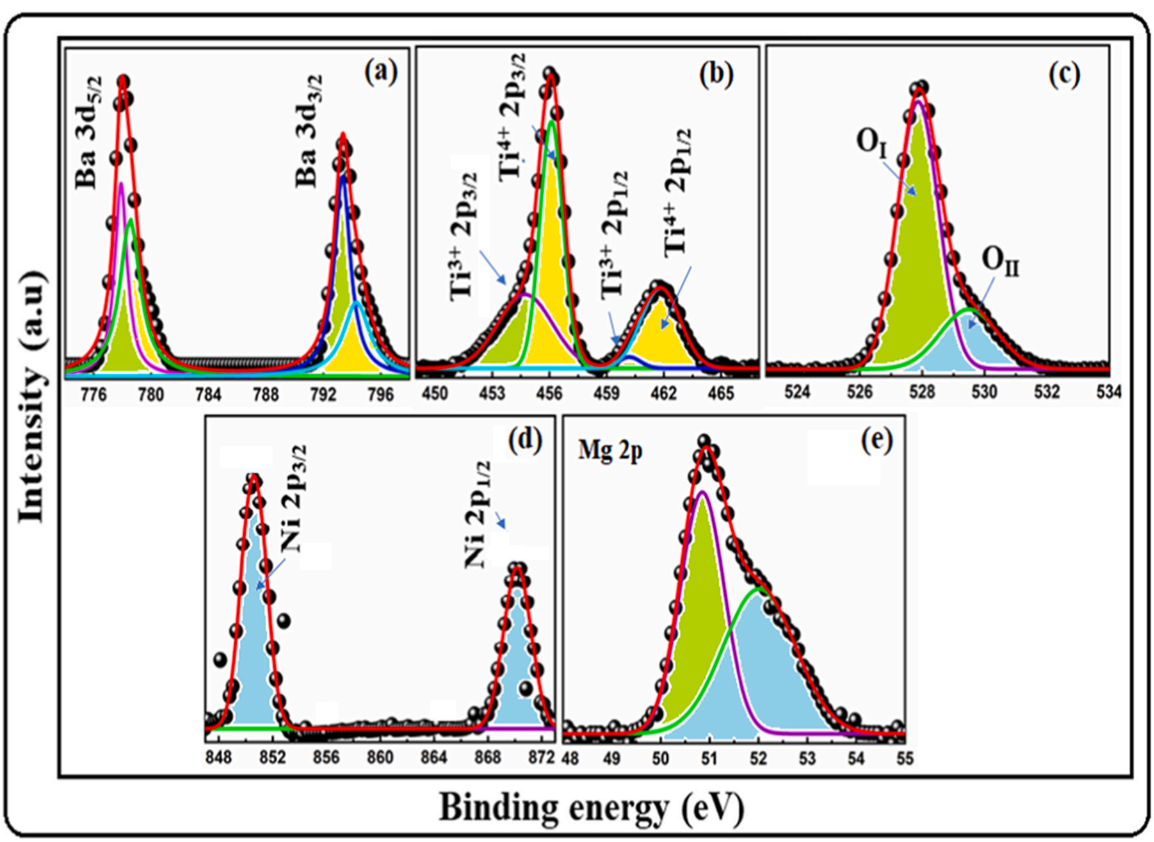

Fig. 5. : High-resolution XPS spectra of (a) Ba 3d, (b) Ti 2p, (c) O 1 s, (d) Ni 2p, and Mg 2p states. The experimental signals (black circles) are fitted with the Lorentzian equation (red-line) for BMNT sample

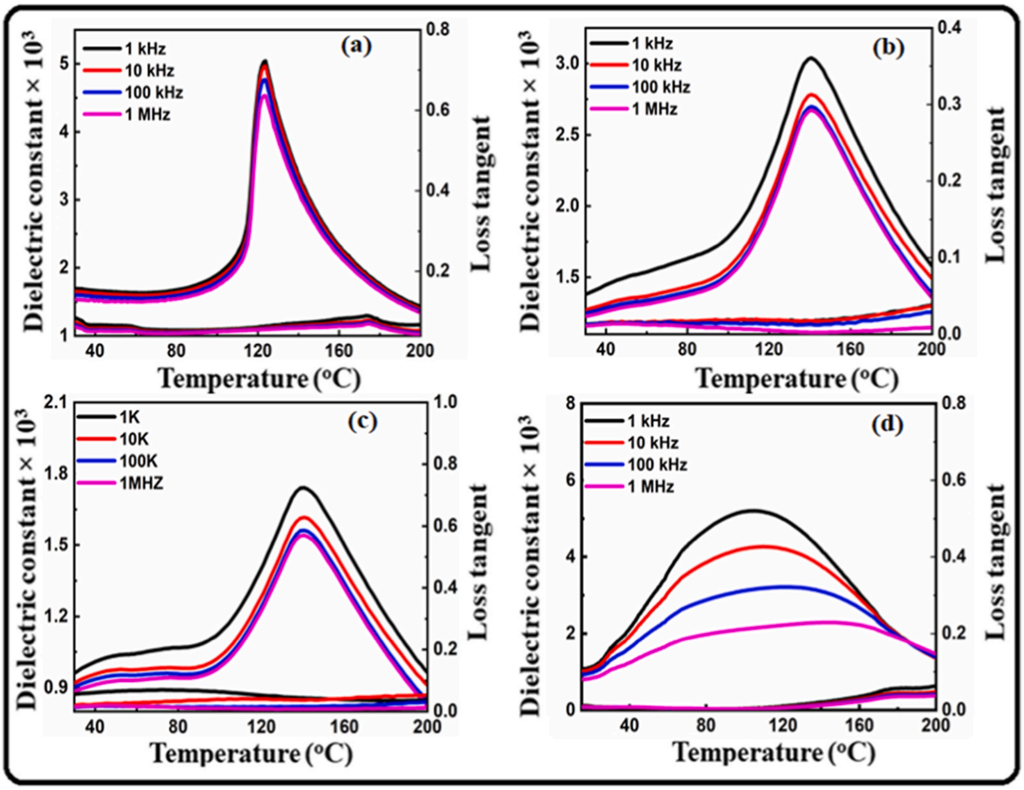

Fig. 6. **:** The dielectric constant (ε_r) and loss tangent of (a) pure BTO, (b) BNCT, (c) BMCT, and (d) BMNT ceramics as a function of temperature and frequency.

BMNT, and a broad peak at 531.22 eV, which may represent chemisorbed species or oxygen vacancy [57]. According to Ni $2p_{1/2}$ and Ni $2p_{3/2}$, shown in Fig. 5(f), the binding energies are 871.2 eV and 855.5 eV, respectively. There is a difference of approximately 15.7 eV between the binding energies of Ni $2p_{1/2}$ and Ni $2p_{3/2}$. This indicates that Ni is a 2 + state [58]. Fig. 5(e) shows a high-resolution scan of Mg 2p core level spectrum consisting of two different electronic states ($2p_{1/2}$, $2p_{3/2}$) corresponding to 48.95 eV and 49.29 eV binding energies, respectively. The difference in the binding energy for both (pure and doped samples) is found to be ~ 0.34 eV. According to the existing literature survey, the peak position and the difference in the binding energy of $2p_{3/2}$ and $2p_{1/2}$ peaks confer that Mg^{2+} ions are present in the 2 + oxidation state [59].

Fig. 6 illustrates the temperature dependency of the dielectric characteristics throughout a temperature range of 30–200 °C and at four distinct frequencies (1 kHz, 10 kHz, 100 kHz, and 1 MHz) (a-d). The sintered samples distinctively show the following features: (i) the sharp phase transition frequently observed in pure $BaTiO_3$ ceramics, which is typical behavior for normal ferroelectrics [60]; (ii) After the (Ni, Cu), (Mg, Cu), and (Ni, Mn) ions were introduced into the BTO lattice, the peak gradually broadens, suggesting the enhanced relaxor behavior, which extends the paraelectric-ferroelectric phase transition over a wide temperature range, was seen in the samples. Numerous factors, including compositional variation [61], micro-polar regions, or coupling of order parameters with local disorder mode over the local strain [62], can lead to the diffused phase transition behavior seen in BNCT, BMCT, and BMNT ceramics. The introduction of two ions in place of Ti^{4+} ions may be what causes the disorder of structure in co-doped materials. Some of the (Ni^{2+}, Cu^{2+}), (Mg^{2+}, Cu^{2+}), and (Mg^{2+}, Ni^{2+}) ions may go to the Ba^{2+} and/or Ti^{4+} sites as well, increasing the compositional variety across nanoscale regions. The diffused phase transition DPT can also emerge from structural instability in the cation arrangement in one or more crystallographic sites, which causes mixtures to be heterogeneous on a nanoscale and, as a result, to have a distribution of different local Curie points [63]. Also, we can see from Fig. 6 that the Curie temperature position is also altered compared to the Curie temperature of the pure sample, which may be related to changes in the grains size [64]. The grain size and grain boundary region of pure are large so that the internal stress can be easily relieved by the grain boundary sliding. At the same time, the samples with co-doping have smaller grain sizes and a lower grain boundary area, which hindered the release of internal tensions and caused variations in the position of the Curie temperature [65]. The relaxor ferroelectric phenomena can be evaluated by the diffuseness factor γ, which is defined via the modified Curie–Weiss law for a relaxor [66,67]:

$$\frac{1}{\varepsilon} - \frac{1}{\varepsilon_m} = \frac{(T - T_m)^{\gamma}}{C} \quad (5)$$

where T_m is the temperature at the maximal dielectric constant (ε_m), and C is the Curie–Weiss constant. For sample BTO, we get $\gamma \sim 1.15$ from the best fitting depicted in Fig. 7(a), demonstrating a typical ferroelectric nature. Indeed, it is found that for the BNCT, BMCT, and BMNT samples, γ gradually increases from 1.15 to 1.56, 1.66, and 1.98, as shown in Fig. 7(b). A significant relaxor for the sample BMNT. It is known that the disordered distribution of Mg^{2+} and Ni^{2+} at the Ti^{4+} -site strengthens the local random fields and causes PNRs, which is the microscopic mechanism behind the relaxor-like behavior [68].

It should be noted that the BMNT sample exhibits properties that are advantageous to energy storage performance. The SEM imaging of the BMNT sample revealed small grains and a dense microstructure, which may cause increased energy storage density. The

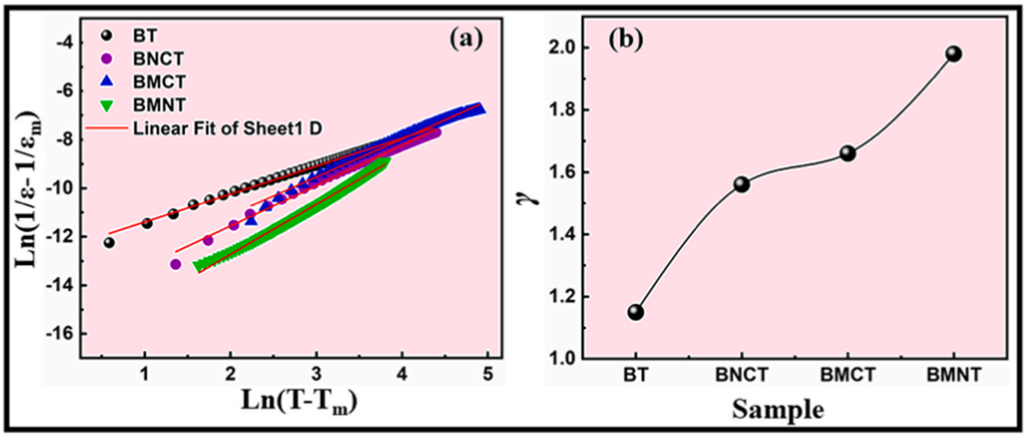

Fig. 7. : (a) Based on the modified Curie-Weiss law, the figure shows a relationship between ln $(1/\varepsilon - 1/\varepsilon_m)$ and ln $(T\text{-}T_m)$ at 1 kHz, and (b) shows the change of degree of diffuseness (γ) with composition in pure and co-doped ceramics

decrease in grain size and crystallite size with Mg^{2+} and Ni^{2+} co-doping further supports the argument that Mg and Ni doping might have raised the micro-regions (which have different Tc) and thus increased the diffused phase nature of the samples. In $BaTiO_3$, oxygen vacancies are created by acceptor co-dopants with 2 + cations. As a result, oxygen octahedra may be distorted. Since the co-dopants have a larger ionic size than Ti [39], the adjacent oxygen will be pushed outward in the direction of (100). Thus, the transition dynamics for polarization are repressed by reducing and delaying the open space for Ti displacement at this axis. As a result, the dielectric response becomes slow, and the phase transition behavior becomes diffused as shown in Fig. 6.

The polarization-electric field (*P-E*) hysteresis loops of pure and (Ni^{2+}, Cu^{2+}), (Mg^{2+}, Cu^{2+}), and (Mg^{2+}, Ni^{2+}) co-doped BTO samples are plotted in Fig. 8(a-d) at ambient temperature. The measurement was performed using f = 10 Hz. As can be seen, the P-E loop for the pure BTO sample displays significant maximum polarization P_{max} values of 26.77 μC/cm^2 and remnant polarization P_r of 15.69 μC/cm^2. The measured P_{max} and P_r are gradually decreased with co-doping (Ni^{2+}, Cu^{2+}), (Mg^{2+}, Cu^{2+}), and (Mg^{2+}, Ni^{2+}), and the *P-E* loop gradually downward, indicating a gradual change from the conventional ferroelectric state to a relaxor-like behavior.

For the pure BTO sample, saturated *P-E* loops are observed for fields approaching 60 kV/cm, but for the co-doped samples, *P-E*

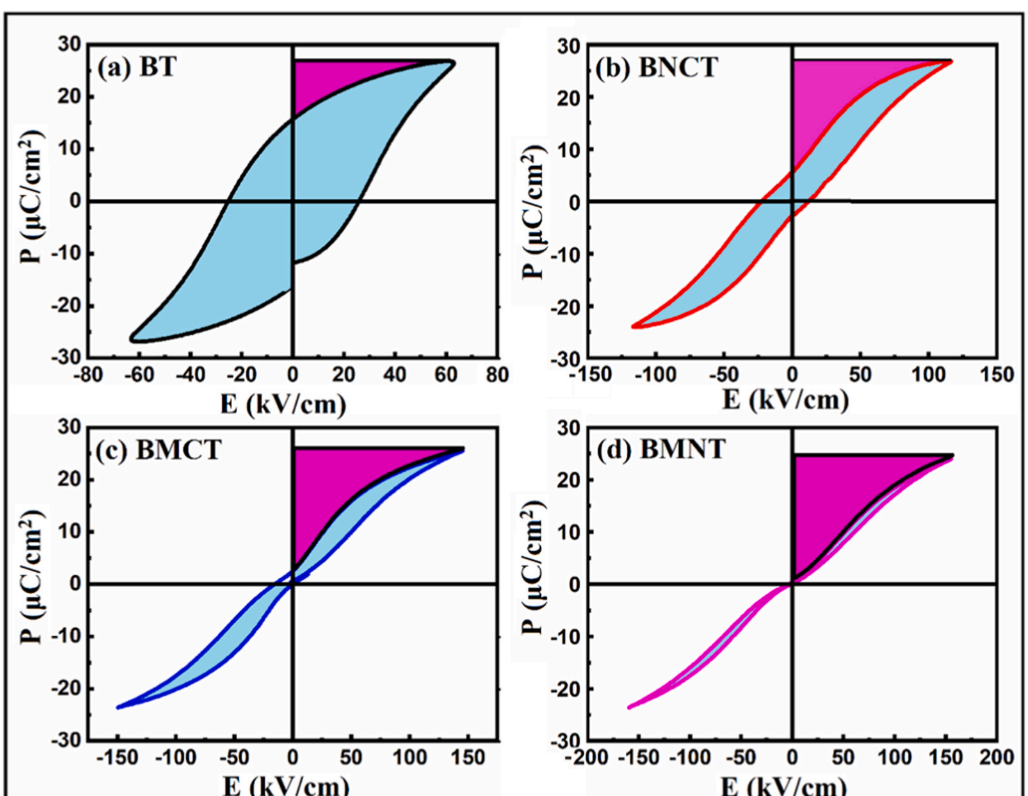

Fig. 8. : shows (a) Bipolar P-E loops of the (a) BTO, (b) BNCT, (c) BMCT, and BMNT ceramic measured at ambient temperatures and 10 Hz frequency.

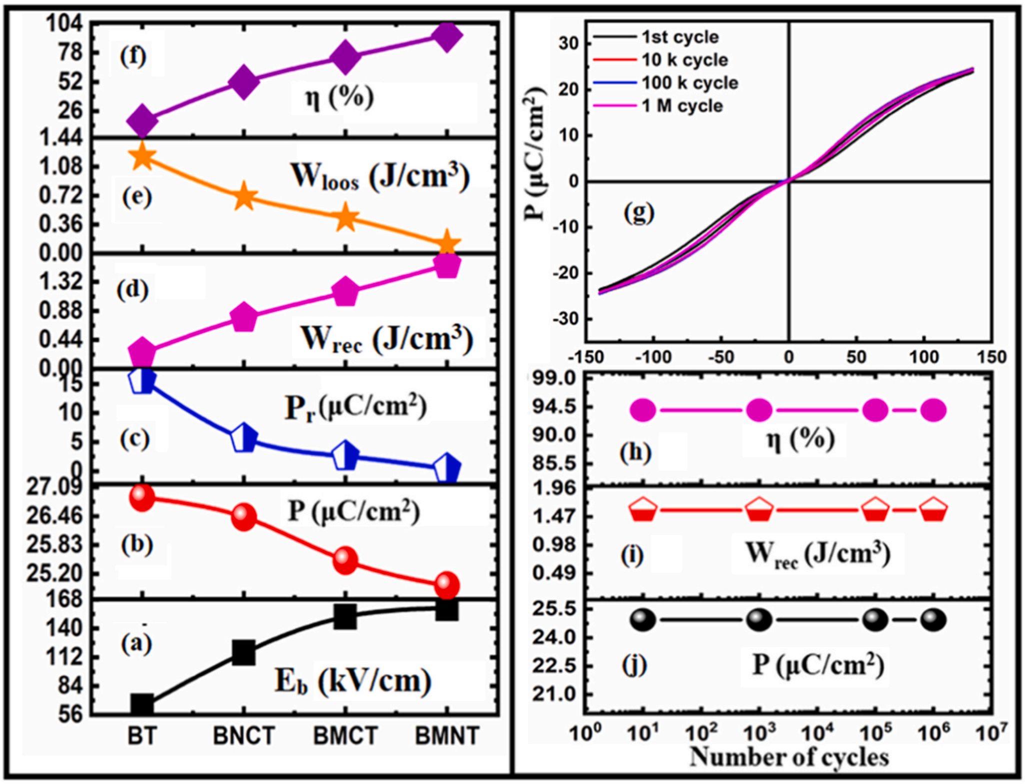

Fig. 9. : shows (a) Breakdown strength Eb, (b) maximum polarization, (c) remnant polarization, (d) energy storage density, (e) Energy loss density which is estimated from the integrated area of the hysteresis loop, (f) energy storage efficiency, (g) After various cycles, the P-E hysteresis loops of BMNT ceramics were measured under E = 140 kV/cm, and f = 50 Hz at room temperature, (h), (i) and (j) represented the stability of the energy storage efficiency, energy storage density and maximum polarization with different cycling number for the optimal BMNT sample.

loops are not saturated even at fields above 100 kV/cm. Furthermore, the *P-E* loop curvature of the BMNT sample indicates a minimal contribution from leakage currents. For confirmation, we measured the *P-E* loops of this sample at different cycling rates at room temperature, as shown in Fig. 9(g). The *P-E* hysteresis loops show almost negligible cycling dependence, indicating the influence of leaky behavior is minimal. To explain this phenomenon based on the acceptor's ions co-doping, as we know the ferroelectric properties of pure BTO ceramics are influenced by compositional modification, microstructure, and lattice defects such as oxygen vacancies. In pure BTO ferroelectric with low defects resulting in neglectable pining effect on the domain walls resulting in enhanced the remnant polarization [Fig. 8(a)]. When the acceptors ions such as Mg^{2+} and Ni^{2+} co-doped Ti^{4+} site of BTO host lattice, the oxygen vacances can be formed, and assemble in the vicinity of domain walls thereby pinning them and making their polarization switching difficult, leading to inhibition in the P_r values [69]. Based on the obtained results and the discussion mentioned above, in the (Ni^{2+}, Cu^{2+}), (Mg^{2+}, Cu^{2+}), and (Mg^{2+}, Ni^{2+}) co-doped BTO samples, the oxygen vacancies accumulate at domain boundaries and walls, resulting in strong domain pinning. Thus, co-doped samples do not exhibit well-saturated *P-E* loops. Moreover, it has been demonstrated that larger grains have relatively free domain walls, increasing P_r values.

As well known, the measured *P-E* loops can be used to study the energy storage properties based on the Eqs. (1) to (3) mentioned in the introduction part, and the obtained energy storage parameters were reported in Table 3.

As seen in Fig. 9, for BNCT, BMCT, and BMNT ceramics, the energy storage density W_{rec} rises from 0.245 J/cm^3 for a pure BTO sample to 0.774, 1.162, and 1.585 J/cm^3. Additionally, the efficiency increases

Table 3
energy storage parameters obtained from knowing the P-E hysteresis loop by assisting Eqs. (1–3) measured at room temperature at 10 Hz. for pure and co-doped samples.

Sample	BTO	BNCT	BMCT	BMNT
Eb (kV/cm)	64.21	116.4	151.35	159.64
P_{max} (μC/cm^2)	26.87	26.44	25.49	24.94
P_r(μC/cm^2)	15.69	05.62	02.57	0.420
W_{rec} (J/cm^3)	0.245	0.774	1.162	1.585
W_{loss}(J/cm^3)	1.206	0.707	0.442	0.107
η (%) ~	17	52	73	94

from 17% for the BTO sample to 52%, 74%, and 94% for the BNCT, BMCT, and BMNT ceramics, respectively. The sample BMNT exhibits the best energy storage performance. The reason behind that could be that incorporating Mg^{2+} and Ni^{2+} into the BTO host lattice enhanced the breakdown strength and relaxor properties. From SEM images, the BMNT sample shows the smallest grain size significantly contributes to the increased breakdown strength E_b, as indicated by an exponential decay relationship with grain size [70]. It is essential to understand that the values of energy storage density and the shape of *P-E* loops significantly depend on the applied field *E*. As shown in Fig. 9(a) and (d), the energy storage density W_{re} is directly proportional to breakdown strength E_b. At the same time, η is only dependent on the shape of the hysteresis loop and entirely independent of E_b for all investigated ceramics. Fig. 9 shows that the high energy storage density is linked with high values of P_{max} and breakdown strength E_b, and small value of P_r. Comparing to pure BTO, the breakdown strength increases but the P_{max} decrease. The BMNT sample shows at the same time high energy storage density and high energy efficiency η.

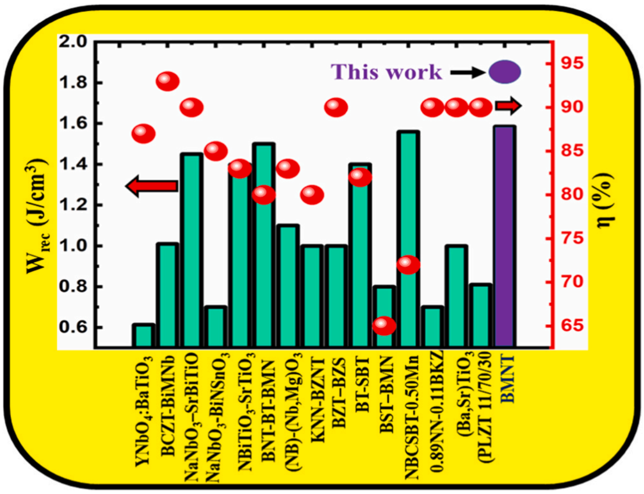

Fig. 10. : W_{rec} and η values of BNBT ceramics compared with values for other lead-free ceramics at the same applied field of around 160 kV/cm [71–85].

It should be noted that the energy storage properties of BMNT ceramics were not reported yet. Thus, a comparison with others for other lead-free ceramics is essential, as shown in Fig. 10 (References [71–85]). The comparison shows that, the energy storage density of BMNT ceramics is 1.585 J/cm^3 and the energy storage efficiency is 94%, which is much better than other samples under investigation. Therefore, this sample was considered an optimum one for our study. To investigate its performance, we subjected it to different cycling at an applied field of 140 kV/cm to avoid the sample braking due to cycling. The obtained *P-E* loops are almost the same shape [Refer to Fig. 9(g)] without any change during different cycling. The corresponding P_{max}, W_{rec}, and efficiency η, W_{rec}, and P_{max}, are shown in Fig. 9(h), (i), and (j), respectively. The results confirmed that energy storage density W_{rec} and efficiency η remain equal at 1.585 J/cm^3 and ~94%, respectively, without any decay. The defect dipoles, small grain size, and dense microstructure are the main contributors to the small hysteresis loop in our sintered sample.

As shown in Fig. 8(a)-(d) above, the *P-E* hysteresis loop was studied at a frequency of 10 Hz to study the cause of the defects-induced effect further. At ambient temperature, the co-doped samples exhibit pinched hysteresis loops, particularly the BMNT sample. The pinching of the hysteresis loops is a signature of the formation of defect dipoles in the BTO host lattice. Additionally, the breakdown strength of the Mg^{2+} and Ni^{2+} co-doped BTO sample increases from 64.21 kV.cm^{-1} to 159.64 kV.cm^{-1}. The significant rise of the breakdown electric field was believed to have resulted from the fine grain size of the Mg^{2+} and Ni^{2+} co-doped BTO ceramics. The defect chemistry provides a more description of this mechanism. The co-doping of Mg^{2+} and Ni^{2+} ions at the Ti^{4+} site of the BTO host lattice resulted in the formation of oxygen vacancies based on defect chemistry and charge compensation mechanisms. In this case, Mg^{2+} and Ni^{2+} form the [$(Mg_{Ti}^{''} - V_O^{\bullet\bullet})$ and $(Ni_{Ti}^{''} - V_O^{\bullet\bullet})$ defect dipoles with neighbouring oxygen vacancies respectively, as illustrated in the schematic diagram in Fig. 11. The literature claims that these defect dipoles can produce a dipole moment (P_d) when an electric field is removed, which may serve as an internal field and cause the domain to return to its initial state, leading to a pinching hysteresis loop [86]. Defect dipoles (P_d) serve as pinning points for polarization switching in their host domains and are typically aligned in the polarization direction. The P_d, which maintains its original orientation, will create a restoring force that forces P_s to revert to their initial state as the applied electric field decreases [86,87]. Once a result, as the applied electric field was reduced, the remnant polarization of BMNT ceramics also decreased dramatically. Consequently, as indicated in the schematic diagram in Fig. 11, the *P-E* loops are pinched. The underlying defect dipoles effect can improve the performance of the energy storage system.

Ultimately, we explain the stability of our optimal BMNT samples at different temperatures and frequencies. It is well known that one of the critical requirements for energy storage devices is temperature stability. At f = 50 Hz and *E* = 150 kV/cm, the unipolar *P-E* loops were measured as a function of T, which ranged from 25 °C to 120 °C,

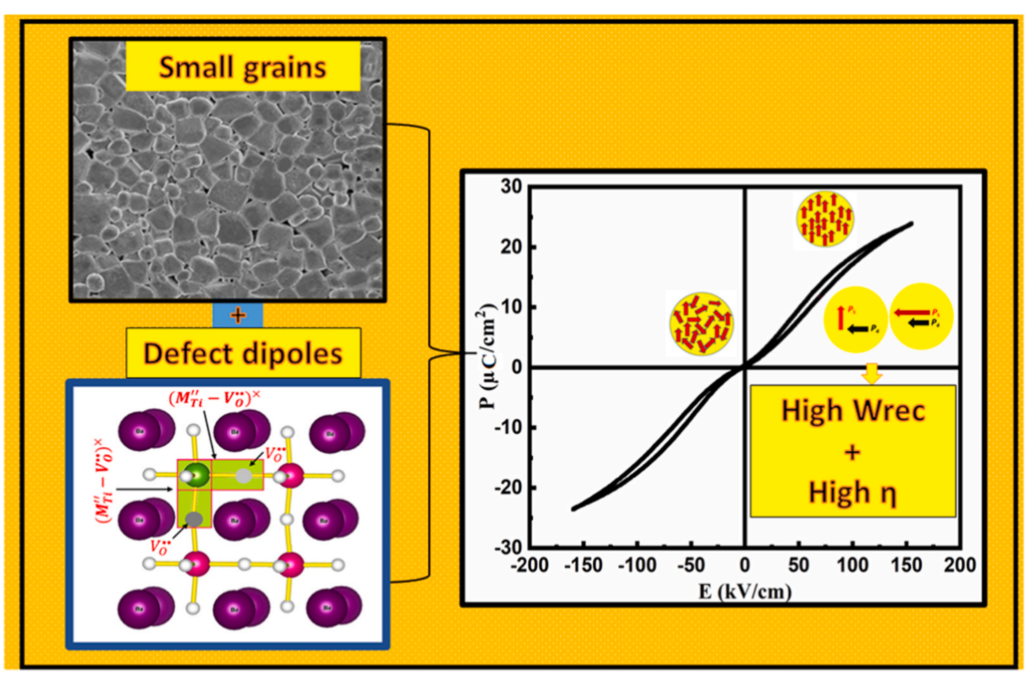

Fig. 11. : Schematic representation of the effect of the grain size and defect dipoles in the ferroelectric and energy storage properties of BMNT ceramics.

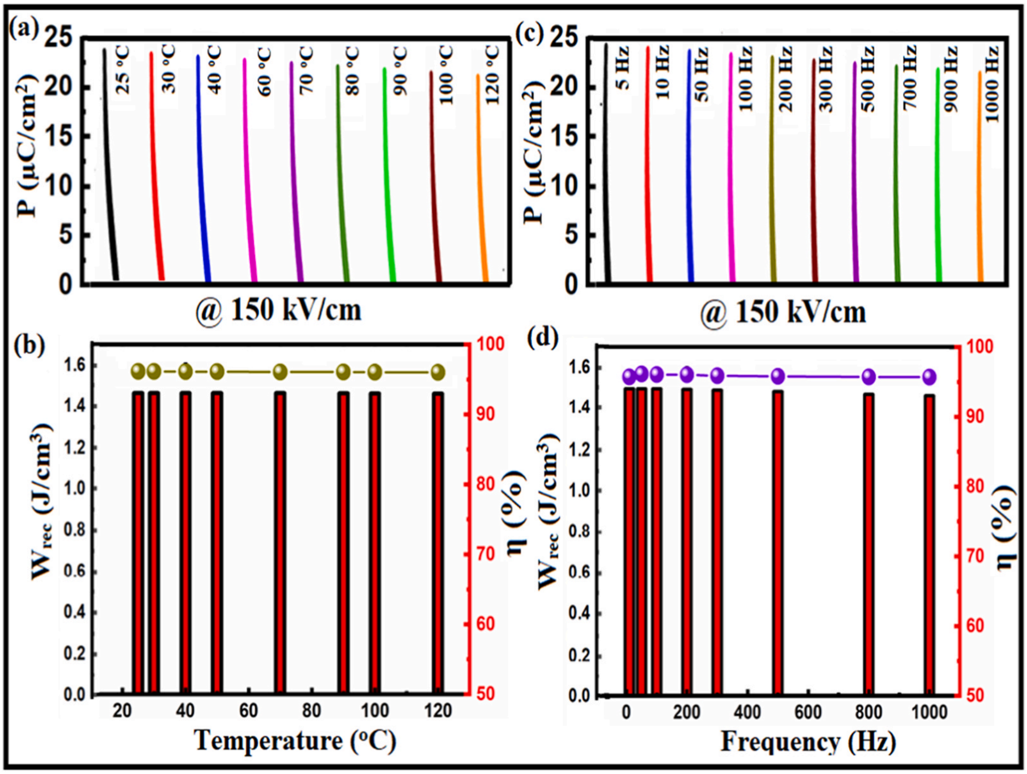

Fig. 12. shows (a) Unipolar P-E loops of the BMNT ceramic measured at different temperatures at 150 kV/cm and 10 Hz frequency. (b) The W_{rec} and η values calculated from (a). (c) Unipolar *P-E* loops of the BMNT ceramic measured at various frequencies at ambient temperature. (d) The W_{rec} and η values calculated from (c).

as shown in Fig. 12. As can be seen, the P_{max} practically remains steady across the examined temperature range. In Fig. 12(b), the relevant W_{rec} and η data are shown. The outcome reveals that W_{rec} and η are unchanged (1.585 J/cm^3 and 94%), respectively. Additionally, as demonstrated in Fig. 12(c) and (d), both Wre and also exhibit good stability with frequency in the range of (1 Hz–1 kHz).

4. Conclusion

In summary, in this study, we made an effort to find a way to obtain an effective storage system that could help to store electrical energy produced from renewable sources and use it when needed. After an extensive study of the previously published literature in pursuit of this goal, our study focused on finding materials that have a high breaking strength (E_b) and a significant difference between (P_{max}) and (P_r) by co-doping the (Ni^{2+}, Cu^{2+}), (Mg^{2+}, Cu^{2+}), and (Mg^{2+}, Ni^{2+}) ions in the BTO host lattice. The results showed that the sample with Mg- and Ni co-doping shows a higher polarization and greater breakdown strength. This behavior was explained based on the effect of grain size and the formation of defective dipoles with neighbouring oxygen vacancies. The domain wall is stabilized by defect dipoles and prevented from moving by oxygen vacancies resulting in a pinched hysteresis loop similar to the double hysteresis loop found in ferroelectric materials. Thus, a high energy storage density and efficiency are produced. At an electric field of 159 kV/cm, the BMNT sample in this study showed an energy storage density (W_{rec}) of 1.585 J/cm^3, which was about 6 times more than that of the net sample, and an efficiency (η) of about 94%. The BMNT sample is exceptionally stable over various temperatures and frequencies, making it a good candidate for applications in future energy storage.

CRediT authorship contribution statement

Mahmoud. S. Alkathy and Attaur Rahaman are in the same contribution: Synthesis, Analysis and interpretation of the data, calculations, visualization, conceptualization, methodology, and writing-original draft. **Valmor Roberto Mastelaro**: Investigation and XPS measurements. **Fabio. L. Zabotto:** Investigation, and spectroscopic characterizations. **Flavio Paulo Milton:** Investigation, and spectroscopic characterizations. **Jose. Antonio. Eiras:** Supervision, writing, correction and approval of the final version. All authors have contributed in preparation of the manuscript.

Data Availability

The data that has been used is confidential.

Declaration of Competing Interest

The authors declare that they have no known competing financial interests or personal relationships that could have appeared to influence the work reported in this paper.

Acknowledgements

The authors would like to acknowledge the experimental facilities provided by CNPq and FAPESP in Grupo de Materiais Ferroicos (GMF), Physics Department/ UFSCar. For financial support, Prof. Dr. Eiras, Dr Alkathy, and Dr. Atta are greatly indebted to the Sao Paulo Research Foundation FAPESP: (Grant no. 2017/13769-1), (Grant no. 2019/03110-8), and (Grant no. 2022/00821-3) respectively.

References

[1] B. Dunn, H. Kamath, J. M, Electrical energy storage for the grid: a battery of choices tarascon, Science 334 (2011) 928–935.

[2] Z.H. Yao, Z. Song, H. Hao, Z.Y. Yu, M.H. Cao, S.J. Zhang, M.T. Lanagan, H.X. Liu, Homogeneous/inhomogeneous-structured dielectrics and their energy-storage performances, Adv. Mater. 29 (2017) 1601727.

[3] Q. Li, L. Chen, M.R. Gadinski, S. Zhang, G. Zhang, H. Li, A. Haque, L. Chen, T. Jackson, Q. Wang, Flexible high-temperature dielectric material from polymer nanocomposites, Nature 523 (2015) 576–579.

[4] Letao Yang, Xi Kong, Fei Li, Hua Hao, Zhenxiang Cheng, Hanxing Liu, Jing-Feng Li, Shujun Zhang, Perovskite lead-free dielectrics for energy storage applications, Prog. Mater. Sci. 102 (2019) 72–108.

[5] Kailun Zou, Yu Dan, Haojie Xu, Qingfeng Zhang, Yinmei Lu, Haitao Huang, Yunbin He, Recent advances in lead-free dielectric materials for energy storage, Mater. Res. Bull. 113 (2019) 190–201.

[6] Ningtao Liu, Ruihong Liang, Zhiyong Zhou, Xianlin Dong, Designing lead-free bismuth ferrite-based ceramics learning from relaxor ferroelectric behavior for simultaneous high energy density and efficiency under low electric field, J. Mater. Chem. C. 6 (38) (2018) 10211–10217.

[7] Gordon R. Love, Energy storage in ceramic dielectrics, J. Am. Ceram. Soc. 73 (2) (1990) 323–328.

[8] Zhen Liu, Teng Lu, Jiaming Ye, Genshui Wang, Xianlin Dong, Ray Withers, Yun Liu, Antiferroelectrics for energy storage applications: a review, Adv. Mater. Technol. 3 (9) (2018) 1800111.

[9] Bingcheng Luo, Xiaohui Wang, Enke Tian, Hongzhou Song, Hongxian Wang, Longtu Li, Enhanced energy-storage density and high efficiency of lead-free $CaTiO_3$–$BiScO_3$ linear dielectric ceramics, ACS Appl. Mater. Interfaces 9 (23) (2017) 19963–19972.

[10] B. Chu, X. Zhou, K. Ren, B. Neese, M. Lin, Q. Wang, F. Bauer, Q.M. Zhang, A dielectric polymer with high electric energy density and fast discharge speed, Science 313 (2006) 334–336.

[11] X.H. Hao, A review on the dielectric materials for high energy-storage application, J. Adv. Dielectr. 3 (2013) 1330001.

[12] H.S. Wang, Y.C. Liu, T.Q. Yang, S.J. Zhang, Ultrahigh energy-storage density in antiferroelectric ceramics with field-induced multiphase transitions, Adv. Funct. Mater. 29 (2019) 1807321.

[13] Guiwei Yan, Liqin Xu, Bijun Fang, Shuai Zhang, Xiaolong Lu, Xiangyong Zhao, Jianning Ding, Achieving high pulse charge-discharge energy storage properties and temperature stability of $(Ba_{0.98-x}Li_{0.02}La_x)(Mg_{0.04}Ti_{0.96})O_3$ lead-free ceramics via bandgap and defect engineering, Chem. Eng. J. 450 (1) (2022) 137814.

[14] L. Yang, X. Kong, F. Li, H. Hao, Z. Cheng, H. Liu, S. Zhang, Perovskite lead-free dielectrics for energy storage applications, Prog. Mater. Sci. 102 (2019) 72–108.

[15] Seungho Cho, Chao Yun, Yoon Seo Kim, Han Wang, Jie Jian, Wenrui Zhang, Jijie Huang, Xuejing Wang, Haiyan Wang, Judith L. MacManus-Driscoll, Strongly enhanced dielectric and energy storage properties in lead-free perovskite titanate thin films by alloying, Nano Energy 45 (2018) 398–406.

[16] H. Ogihara, C.A. Randall, S. Trolier-McKinstry, High-energy density capacitors utilizing $0.7BaTiO_3$–$0.3BiScO_3$ ceramics, J. Am. Ceram. Soc. 92 (2009) 1719–1724.

[17] H. Pan, J. Ma, J. Ma, Q. Zhang, X. Liu, B. Guan, L. Gu, X. Zhang, Y.J. Zhang, L. Li, Y. Shen, Y.H. Lin, C.W. Nan, Giant energy density and high efficiency achieved in bismuth ferrite-based film capacitors via domain engineering, Nat. Commun. 9 (2018) 1813.

[18] Biaolin Peng, Qi Zhang, Xing Li, Tieyu Sun, Huiqing Fan, Shanming Ke, Mao Ye, et al., Giant electric energy density in epitaxial lead-free thin films with coexistence of ferroelectrics and antiferroelectrics, Adv. Electron. Mater. 1 (2015) 1500052.

[19] H. Pan, S. Lan, S. Xu, Q. Zhang, H. Yao, Y. Liu, F. Meng, E.J. Guo, L. Gu, D. Yi, X. Renshaw Wang, Ultrahigh energy storage in superparaelectric relaxor ferroelectrics, 2021, Science 374 (6563) (2021) 100–104.

[20] H. Pan, A. Kursumovic, Y.-H. Lin, C.-W. Nan, J.L. MacManus-Driscoll, Dielectric films for high performance capacitive energy storage: multiscale engineering, Nanoscale 12 (2020) 19582–19591.

[21] Xi Dong, Hongwei Chen, Meng Wei, Kaituo Wu, Jihua Zhang, Structure, dielectric and energy storage properties of $BaTiO_3$ ceramics doped with $YNbO_4$, J. Alloy. Compd. 744 (2018) 721–727.

[22] Shujuan Liu, Qidong Xie, Lixue Zhang, Yingying Zhao, Xuan Wang, Pu Mao, Jiping Wang, Xiaojie Lou, Tunable electrocaloric and energy storage behavior in the Ce, Mn hybrid doped $BaTiO_3$ ceramics, J. Eur. Ceram. Soc. 38 (4) (2018) 4664–4669.

[23] G.W. Yan, M.G. Ma, C.B. Li, Z.W. Li, X.Y. Zhong, J. Yang, F. Wu, Z.H. Chen, Enhanced energy storage property and dielectric breakdown strength in Li+ doped $BaTiO_3$ ceramics, Alloy. Compd. 857 (2021) 158021.

[24] Wenfeng Liu, Jinghan Gao, Yi Zhao, Shengtao Li, Significant enhancement of energy storage properties of BaTiO3-based ceramics by hybrid-doping, Alloy. Compd. 843 (2020) 155938.

[25] G. Liu, L. Zhang, Q. Wu, Z. Wang, Y. Li, D. Li, H. Liu, Y. Yan, Enhanced energy storage properties in MgO-doped $BaTiO_3$ lead-free ferroelectric ceramics, J. Mater. Sci: Mater. Electron 29 (21) (2018) 18859–18867.

[26] M.X. Zhou, R.H. Liang, Z.Y. Zhou, X.L. Dong, Novel $BaTiO_3$-based lead-free ceramic capacitors featuring high energy storage density, high power density, and excellent stability, J. Mater. Chem. C. 6 (2018) 8528–8537.

[27] D. Meng, Q. Feng, M. Wang, N.N. Luo, X.Y. Chen, X. Liu, C.L. Yuan, Y.Z. Wei, T. Fujita, H. You, Realising high comprehensive energy storage performance of $BaTiO_3$-based perovskite ceramics via $La(Zn_{1/2}Hf_{1/2})O_3$ modification, Ceram. Int. 48 (2022) 16173–16182.

[28] Wen-Bo Li, Di Zhou, Li-Xia Pang, Enhanced energy storage density by inducing defect dipoles in lead free relaxor ferroelectric BaTiO3-based ceramics, Appl. Phys. Lett. 110 (13) (2017) 132902.

[29] W. Cao, W. Li, Y. Feng, T. Bai, Y. Qiao, Y. Hou, T. Zhang, Y. Yu, W. Fei, Defect dipole induced large recoverable strain and high energy-storage density in lead-free Na0. 5Bi0. 5TiO3-based systems, Appl. Phys. Lett. 108 (20) (2016) 202902.

[30] Jia-Han Zhang, Zhou Zhou, Jiean Li, Bingzhong Shen, Tangsong Zhu, Xingxun Gao, Ruowen Tao, et al., Coupling enhanced performance of triboelectric–piezoelectric hybrid nanogenerator based on nanoporous film of poly (vinylidene fluoride)/$BaTiO_3$ composite electrospun fibers, ACS Mater. Lett. 4 (5) (2022) 847–852.

[31] Yu Huang, Hui Bing, Liu Xiao, Qiang Liu, Juan Li, Yong Jun Wu, Defect dipoles induced high-energy storage density in Mn-doped BST ceramics prepared by spark plasma sintering, J. A. Ceram. Soc. 102 (4) (2019) 1904–1911.

[32] Y. Zhao, B. Yang, Y. Liu, Y. Zhou, Q. Wu, S. Zhao, Capturing carriers and driving depolarization by defect engineering for dielectric energy storage, ACS Appl. Mater. Interfaces 14 (5) (2022) 6547–6559.

[33] Yulei Zhang, Weili Li, Zhenyu Wang, Yulong Qiao, Hetian Xia, Ruixuan Song, Yu Zhao, Weidong Fei, Perovskite $Sr_{1-x}(Na_{0.5}Bi_{0.5})_xTi_{0.99}Mn_{0.01}O_3$ thin films with defect dipoles for high energy-storage and electrocaloric performance, ACS Appl. Mater. Interfaces 11 (41) (2019) 37947–37954.

[34] Ying Zhang, Ang Li, Ganrong Zhang, Yingqiu Zheng, Aojun Zheng, Guoqiang Luo, Rong Tu, Yi Sun, Jian Zhang, Qiang Shen, Optimization oF Energy Storage Properties in Lead-free Barium Titanate-based Ceramics via B-site defect dipole engineering, ACS Sustain. Chem. Eng. 10 (9) (2022) 2930–2937.

[35] Hongye Wang, Rui Huang, Cheng Tao, Hua Hao, Zhonghua Yao, Hanxing Liu, Minghe Cao, Defect controlling of $BaTiO_3$@ NiO double hysteresis loop ceramics with enhanced energy storage capability and stability, J. Eur. Ceram. Soc. 42 (5) (2022) 2212–2220.

[36] F. Yang, S. Bao, Y. Zhai, Y. Zhang, Z. Su, J. Liu, J. Zhai, Z. Pan, Enhanced energy-storage performance and thermal stability in $Bi_{0.5}Na_{0.5}TiO_3$-based ceramics through defect engineering and composition design, Mater. Today Chem. 22 (2021) 100583.

[37] A. Jain, Y. Wang, H. Guo, Emergence of relaxor behavior along with enhancement in energy storage performance in light rare-earth doped $Ba_{0.90}Ca_{0.10}Ti_{0.90}Zr_{0.10}O_3$ ceramics, Ceram. Int. 47 (2020) 10590–10602.

[38] Min-Jia Wang, Hui Yang, Qi-Long Zhang, Zhi-Sheng Lin, Zi-Shan Zhang, Dan Yu, Liang Hu, Microstructure and dielectric properties of $BaTiO_3$ ceramic doped with yttrium, magnesium, gallium and silicon for AC capacitor application, Mater. Res. Bull. 60 (2014) 485–491.

[39] R.D. Shannon, Revised effective ionic radii and systematic studies of interatomic distances in halides and chalcogenides, Acta Crystallogr 32 (5) (1976) 751–767.

[40] U. Holzwarth, N. Gibson, The Scherrer equation versus the 'Debye-Scherrer equation, Nat. Nanotechnol. 6 (9) (2011) 534.

[41] Devendra Singh, Anju Dixit, P.S. Dobal, Ferroelectricity and ferromagnetism in Fe-doped barium titanate ceramics, Ferroelectrics 573 (1) (2021) 63–75.

[42] G. Schileo, L. Luisman, A. Feteira, M. Deluca, K. Reichmann, 'Structure–property relationships in $BaTiO_3$-$BiFeO_3$–$BiYbO_3$ ceramics, J. Eur. Ceram. Soc. 33 (2013) 1457–1468.

[43] F. Maxim, P. Ferreira, P.M. Vilarinho, I. Reaney, Hydrothermal synthesis and crystal growth studies of $BaTiO_3$ using Ti nanotube precursors, Cryst. Growth Des. 8 (9) (2008) 3309–3315.

[44] Z. Raddaoui, B. Smiri, A. Maaoui, J. Dhahri, R.M. ghaieth, N. Abdelmoula, K. Khiroun, Correlation of crystal structure and optical properties of $Ba_{0.97}Nd_{0.0267}Ti_{(1-x)}W_xO_3$ perovskite, RSC Adv. 8 (2018) 27870.

[45] T. Mondal, S. Das, T. Badapanda, T.P. Sinha, P.M. Sarun, Effect of Ca2+ substitution on impedance and electrical conduction mechanism of $Ba_{1-x}Ca_xZr_{0.1}Ti_{0.9}O_3$ ($0.00 \le x \le 0.20$) ceramics, Phys. B 508 (2017) 124–135.

[46] V. Sanjay Kumar Upadhyay, Raghavendra Reddy, N. Lakshmi, Study of (1−x) $BaTiO_3$-$xNi_{0.5}Zn_{0.5}Fe_2O_4$ (x =5, 10 and 15%) magneto-electric ceramic composites, J. Asian Ceram. Soc. 1 (4) (2013) 346–350.

[47] V. Pal, O.P. Thakur, R.K. Dwivedi, Investigation of MPB region in lead free BLNT-BCT system through XRD and Raman spectroscopy, J. Phys. D. Appl. Phys. 48 (2015) 055301.

[48] J. Kreisel, A.M. Glazer, G. Jones, P.A. Thomas, L. Abello, G. Lucazeau, An x-ray diffraction and Raman spectroscopy investigation of A-site substituted perovskite compounds: the $(Na_{1-x}K_x)_{0.5}Bi_{0.5}TiO_3$ ($0 \le x \le 1$) solid solution, J. Phys. Condens. Matter 12 (2000) 3267.

[49] J. Petzelt, S. Kamba, J. Fábry, D. Noujni, V. Porokhonskyy, A. Pashkin, G.E. Kugel, Infrared, Raman and high-frequency dielectric spectroscopy and the phase transitions in $Na_{1/2}Bi_{1/2}TiO_3$, J. Phys. Condens. Matter 16 (15) (2004) 2719–2731.

[50] J. Kreisel, A. Glazer, P. Bouvier, G. Lucazeau, High-pressure Raman study of a relaxor ferroelectric: the $Na_{0.5}Bi_{0.5}TiO_3$ perovskite, Phys. Rev. B 63 (2001) 174106.

[51] J. Ma, J. Gu, D. Su, X.M. Wu, C.H. Song, W. Li, X.M. Lu, J.S. Zhu, Structural and ferroelectric properties of yttrium substituted bismuth titanium thin films, Thin Solid films 492 (2005) 264–268.

[52] X. Yang, D. Li, Z.H. Ren, R.G. Zeng, S.Y. Gong, D.K. Zhou, H. Tian, J.X. Li, G. Xu, Z.J. Shen, G.R. Han, The Colossal dielectric performance of pure barium titanate ceramics consolidated by spark plasma sintering, RSC Adv. 6 (2016) 75422.

[53] Bedri Erdem, Robert A. Hunsicker, Gary W. Simmons, E. David Sudol, Victoria L. Dimonie, Mohamed S. El-Aasser, XPS and FTIR surface characterization of TiO_2 particles used in polymer encapsulation, Langmuir 17 (9) (2001) 2664–2669.

[54] Mahmoud S. Alkathy, Fabio L. Zabotto, Flavio Paulo Milton, J.A. Eiras, Bandgap tuning in samarium-modified bismuth titanate by site engineering using iron and cobalt co-doping for photovoltaic application, J. Alloy. Compd. 908 (2022) 164222.
[55] Mahmoud S. Alkathy, L.Zabotto Fabio, K.C.James Raju, J.A. Eiras, Effect of defects on the band gap and photoluminescence emission of Bi and Li co-substituted barium strontium titanate ceramics, Mater. Chem. Phys. 275 (2022) 125235.
[56] X. Ren, Large electric-field-induced strain in ferroelectric crystals by point-defect-mediated reversible domain switching, Nat. Mater. 3 (2004) 91–94.
[57] Agda Eunice Souza, Silvio Rainho Teixeira, Cassio Morilla-Santos, Wido Herwig Schreiner, Paulo Noronha Lisboa Filho, Elson Longo, Photoluminescence activity of $Ba_{1-x}Ca_xTiO_3$: dependence on particle size and morphology, J. Mater. Chem. C. 2 (34) (2014) 7056–7070.
[58] J. Tian, H. Gao, H. Kong, P. Yang, W. Zhang, J. Chu, Influence of transition metal doping on the structural, optical, and magnetic properties of TiO_2 films deposited on Si substrates by a sol–gel process, Nano Res. Lett. 8 (2013) 533.
[59] N. Rani, S. Chahal, P. Kumar, et al., Role of oxygen vacancies for mediating ferromagnetic ordering in La-doped MgO nanoparticles, J. Supercond. Nov. Magn. 33 (2020) 1473–1480.
[60] Mahamoud S. Alkathy, K.C. James Raju, Study of diffuse phase transition behaviour in Bi and Li Co-substituted barium titanate ceramics, J. Electroceram. 38 no. 1 (2017) 63–73.
[61] Feng Li, Kai Li, Mingsheng Long, Chunchang Wang, Guohua Chen, Jiwei Zhai, Ferroelectric-relaxor crossover induce large electrocaloric effect with ultrawide temperature span in NaNbO3-based lead-free ceramics, Appl. Phys. Lett. 118 (4) (2021) 043902.
[62] E.V. Ramana, N.M. Ferreira, A. Mahajan, D.M. Tobaldi, I. Bdikin, B. Rožič, Z. Kutnjak, M.A. Valente, Processing mediated enhancement of ferroelectric and electrocaloric properties in $Ba(Ti_{0.8}Zr_{0.2})O_3$–$(Ba_{0.\ 7}Ca_{0.\ 3})TiO_3$ lead-free piezoelectrics, Eur. Ceram. Soc. 41 (13) (2021) 6424–6440.
[63] Tio Putra Wendari, Mukhniyal Ikhram, Yulia Eka Putri, Upita Septiani, Enhanced dielectric and ferroelectric responses in La^{3+}/Ti^{4+} co-substituted $SrBi_2Ta_2O_9$ Aurivillius phase, Ceram. Int. 48 (7) (2022) 10328–10332.
[64] Sapna Kumari, Amit Kumar, Aman Kumar, V. Kumar, Vikas N. Thakur, Ashok Kumar, P.K. Goyal, Anurag Gaur, Anil Arya, A.L. Sharma, Enhanced Curie temperature and superior temperature stability by site selected doping in BCZT based lead-free ceramics, Ceram. Int. 48 (10) (2022) 13780–13793.
[65] T. Hiroshima, K. Tanaka, T. Kimura, Effect of microstructure and composition on curie temperature of lead barium niobate solid solution, J. A. Ceram. Soc. 79 (12) (1996) 3235–3242.
[66] K. Uchino, S. Nomura, Critical exponents of the dielectric constants in diffused-phase-transition crystals, Ferroelectrics 44 (1982) 55–61.
[67] Jalel Massoudi, Olfa Messaoudi, Sirine Gharbi, Taoufik Mnasri, Essebti Dhahri, Kamel Khirouni, El. Kebir Hlil, Latifah Alfhaid, Leila Manai, Arwa Azhary, Magnetocaloric effect, dielectric relaxor behavior, and evidence for direct magnetodielectric behavior in $Ni_{0.6}Zn_{0.4}Al_{0.5}Fe_{1.5}O_4$ ceramics for high-temperature applications, J. Mater. Chem. C 126 (5) (2022) 2857–2867.
[68] A. Pramanick, S. Nayak, Perspective on emerging views on microscopic origin of relaxor behavior, J. Mater. Res. 36 (5) (2021) 1015–1036.
[69] I. Coondoo, N. Panwar, A.K. Jha, Effect of sintering temperature on the structural, dielectric and ferroelectric properties of tungsten substituted SBT ceramics, Phys. B Condens. Matter 406 (3) (2011) 374–381.
[70] Gui-wei Yan, Ming-gang Ma, Cheng-bo Li, Zhi-wei Li, Xiao-yu Zhong, Jian Yang, Fei Wu, Zhi-hui Chen, Enhanced energy storage property and dielectric breakdown strength in Li+ doped $BaTiO_3$ ceramics, J. Alloy. Compd. 857 (2021) 158021.
[71] Xi Dong, Hongwei Chen, Meng Wei, Kaituo Wu, Jihua Zhang, Structure, dielectric and energy storage properties of $BaTiO_3$ ceramics doped with YNbO4, J. Alloy. Compd. 744 (2018) 721–727.
[72] Z. Dai, J. Xie, Z. Chen, S. Zhou, J. Liu, W. Liu, Z. Xi, X. Ren, Improved energy storage density and efficiency of $(1-x)Ba_{0.85}Ca_{0.15}Zr_{0.1}Ti_{0.9}O_3$-$xBiMg_{2/3}Nb_{1/3}O_3$ lead-free ceramics, Chem. Eng. J. 410 (2021) 128341.
[73] Tian Wei, Kai Liu, Pengyuan Fan, Daju Lu, Baohua Ye, Changrong Zhou, Huabing Yang, et al., Novel $NaNbO_3$–$Sr_{0.7}Bi_{0.2}TiO_3$ lead-free dielectric ceramics with excellent energy storage properties, Ceram. Int 47 (3) (2021) 3713–3719.
[74] X. Dong, X. Li, X. Chen, H. Chen, C. Sun, J. Shi, H. Zhou, High energy storage density and power density achieved simultaneously in $NaNbO_3$-based lead-free ceramics via antiferroelectricity enhancement, J. Mater. 7 (3) (2021) 629–639.
[75] L.I. Tianyu, et al., Energy storage performance of $Na_{0.5}Bi_{0.5}TiO_3$-$SrTiO_3$ lead-free relaxor modified by $AgNb_{0.85}Ta_{0.15}O_3$, J. Chem. Eng. 406 (2021) 127151.
[76] Biao Guo, Yan Yan, Mingyang Tang, Ziyang Wang, Yang Li, Leiyang Zhang, Haibo Zhang, Li Jin, Gang Liu, Energy storage performance of $Na_{0.5}Bi_{0.5}TiO_3$ based lead-free ferroelectric ceramics prepared via non-uniform phase structure modification and rolling process, J. Chem. Eng. 420 (2021) 130475.
[77] J. Jiang, X. Meng, L. Li, J. Zhang, S. Guo, J. Wang, S.T. Zhang, Enhanced energy storage properties of lead-free NaNbO3-based ceramics via A/B-site substitution, J. Chem. Eng. 422 (2021) 130130.
[78] M. Zhang, H. Yang, Y. Yu, Y. Lin, Energy storage performance of $K_{0.5}Na_{0.5}NbO_3$-based ceramics modified by $Bi(Zn_{2/3}(Nb_{0.85}Ta_{0.15})_{1/3})O_3$, J. Chem. Eng. 425 (2021) 131465.
[79] X. Lin, X. Zhao, L. Zhou, et al., Novel barium zirconate titanate-based lead-free ceramics with stably high energy storage performance over a broad temperature and frequency range, J. Mater. Sci: Mater. Electron 32 (2021) 11845–11856.
[80] Gang Liu, Yang Li, Biao Guo, Mingyang Tang, Quan Li, Jia Dong, Linjiang Yu, et al., Ultrahigh dielectric breakdown strength and excellent energy storage performance in lead-free barium titanate-based relaxor ferroelectric ceramics via a combined strategy of composition modification, viscous polymer processing, and liquid-phase sintering, Chem. Eng. J. 398 (2020) 125625.
[81] Z. Dai, J. Xie, W. Liu, X. Wang, L. Zhang, Z. Zhou, J. Li, X. Ren, Effective strategy to achieve excellent energy storage properties in lead-free $BaTiO_3$-based bulk ceramics, ACS Appl. Mater. Interfaces 12 (27) (2020) 30289–30296.
[82] J. Fang, T. Wang, K. Li, Y. Li, W. Gong, Energy storage properties of Mn-modified $(Na_{0.2}Bi_{0.2}Ca_{0.2}Sr_{0.2}Ba_{0.2})TiO_3$ high-entropy relaxor-ferroelectric ceramics, Results Phys. 38 (2022) 105617.
[83] Aiwen Xie, Jian Fu, Ruzhong Zuo, Achieving stable relaxor antiferroelectric P phase in $NaNbO_3$-based lead-free ceramics for energy-storage applications, J. Mater. 8 (3) (2022) 618–626.
[84] Wei Huang, Ying Chen, Xin Li, Genshui Wang, Jiake Xia, Xianlin Dong, Superior energy storage performances achieved in $(Ba,Sr)TiO_3$-based bulk ceramics through composition design and Core-shell structure engineering, Chem. Eng. J. 444 (2022) 135523.
[85] A. Kumar, S.H. Kim, A. Thakre, et al., Increased energy-storage density and superior electric field and thermally stable energy efficiency of aerosol-deposited relaxor $(Pb_{0.89}La_{0.11})(Zr_{0.70}Ti_{0.30})O_3$ Films, J. Therm. Spray. Tech. 30 (2021) 591–602.
[86] Zhi-Hao Zhao, Yejing Dai, Feng Huang, The formation and effect of defect dipoles in lead-free piezoelectric ceramics: a review, Sustain. Mater. Technol. 20 (2019) e00092.
[87] J. Shi, Y. Zhao, J. He, T. Li, F. Zhu, W. Tian, X. Liu, Deferred polarization saturation boosting superior energy-storage efficiency and density simultaneously under moderate electric field in relaxor ferroelectrics, ACS Appl. Energy Mater. 5 (3) (2022) 3436–3446.